

# Geophysical Research Letters

## RESEARCH LETTER

10.1029/2020GL087361

### Key Points:

- Yutu-2 encountered several abnormally fresh craters surrounded by blocky fragments
- Radar permittivity of the blocky ejecta is not distinct from nearby normal regolith
- The small craters are likely secondaries, and impact compaction occurred in regolith

### Supporting Information:

- Supporting Information S1

• Figure S1

• Figure S2

• Figure S3

• Figure S4

• Figure S5

### Correspondence to:

Z. Xiao,  
xiaozhiyong@mail.sysu.edu.cn

### Citation:







Ding, C., Xiao, Z., Wu, B., Li, Y., Prieur, N. C., Cai, Y., et al. (2020). Fragments delivered by secondary craters at the Chang'e 4 landing site. *Geophysical Research Letters*, 47, e2020GL087361. <https://doi.org/10.1029/2020GL087361>

Received 2 FEB 2020

Accepted 23 MAR 2020

Published online 0

## Fragments Delivered by Secondary Craters at the Chang'E-4 Landing Site

Chunyu Ding<sup>1</sup> , Zhiyong Xiao<sup>1,2,3</sup> , Bo Wu<sup>4</sup> , Yuan Li<sup>4</sup>, Nils C. Prieur<sup>5</sup> , Yuzhen Cai<sup>1</sup> , Yan Su<sup>6</sup>, and Jun Cui<sup>1,3,6</sup> 

<sup>1</sup>Planetary Environmental and Astrobiological Laboratory, School of Atmospheric Sciences, Sun Yat-sen University, Zhuhai, China, <sup>2</sup>State Key Laboratory of Lunar and Planetary Sciences, Space Science Institute, Macau University of Science and Technology, Macau, China, <sup>3</sup>Center for Excellence in Comparative Planetology, Chinese Academy of Science, Hefei, China, <sup>4</sup>Department of Land Surveying and Geo-Informatics, The Hong Kong Polytechnic University, Hong Kong, <sup>5</sup>Centre for Earth Evolution and Dynamics, University of Oslo, Oslo, Norway, <sup>6</sup>Key Laboratory of Lunar and Deep Space Exploration, National Astronomical Observatories, Beijing, China

**Abstract** The Chang'E-4 landing site is depleted with boulders seen from both orbit and surface. However, the Yutu-2 rover came across thousands of concreted fragments in and around an abnormally fresh crater that has more elevated northwestern rims. The origin of the fragments is crucial to resolve the provenances of surface materials detected by the rover. The lunar penetrating radar performed two in-and-out scans for the blocky ejecta, revealing that the subsurface materials have indistinguishable radar permittivity with the surrounding regolith. Forward modeling of electromagnetic wave propagation shows that the fragments were not an original component in the subsurface. This crater is among the several fresh craters photoed by the rover, and they are located in an eastern extension ray of the Zhinyu crater. The small craters are likely secondaries of Zhinyu, and the fragments contain a mixture of shattered projectiles and most likely compacted regolith clumps formed during the secondary impacts.

**Plain Language Summary** The Chang'E-4 landing site lacks boulders seen from both orbit and surface, but several abnormally fresh craters were encountered by the Yutu-2 rover. The blocky rims and interiors are in sharp contrast with the heavily degraded crater population in the landing area. These craters are less than 3 m in diameter, and the fragments are less than 10 cm long and appear earthy in color. The origin of the fragments needs an explanation because it is the basis for the interpretation of data returned by both the lunar penetrating radar and reflectance spectrometer onboard the rover. At the ninth lunar day, the rover was carefully driven into the blocky ejecta deposits of such a crater, and ground-penetrating radar detections were conducted. Radar measurements reveal that the physical properties beneath the blocky ejecta deposits are essentially the same with that of the surrounding regolith, and the observed fragments were not originated from the subsurface. The high spatial density, more pronounced northwestern rims, and colocation with an impact ray suggest that the small craters are most likely secondaries formed by the Zhinyu crater. The fragments are mainly formed by impact compaction of the preimpact target regolith, and the shattered secondaries-forming projectiles are a minor component.

## 1. Introduction

The landing site of the Chang'E-4 mission is located on an Imbrian-aged mare surface on the lunar farside (~3.6 billion years old; Huang et al., 2018), on the floor of the Von Kármán crater (Figure 1a). The location of the landing area within the largest impact basin on the Moon, the South Pole-Aitken basin, makes the study of surface composition particularly interesting. Secondaries delivered by various craters have covered the entire landing area, so that the Yutu-2 rover might encounter not only the Imbrian-aged mare materials along its path but also highland materials ejected from impact craters outside of the Von Kármán crater (Huang et al., 2018). Finding surface materials that were sourced from lunar interior, analyzing their composition, and resolving their origins could be a key to reveal the possible structure and composition of the lunar interior (Wu et al., 2019).

Since being deployed from the lander to the lunar surface, the Yutu-2 rover has explored a distance of over 330 m across 12 lunar days (Figure 1b). Images returned by both the lander and rover in the first 5 lunar days

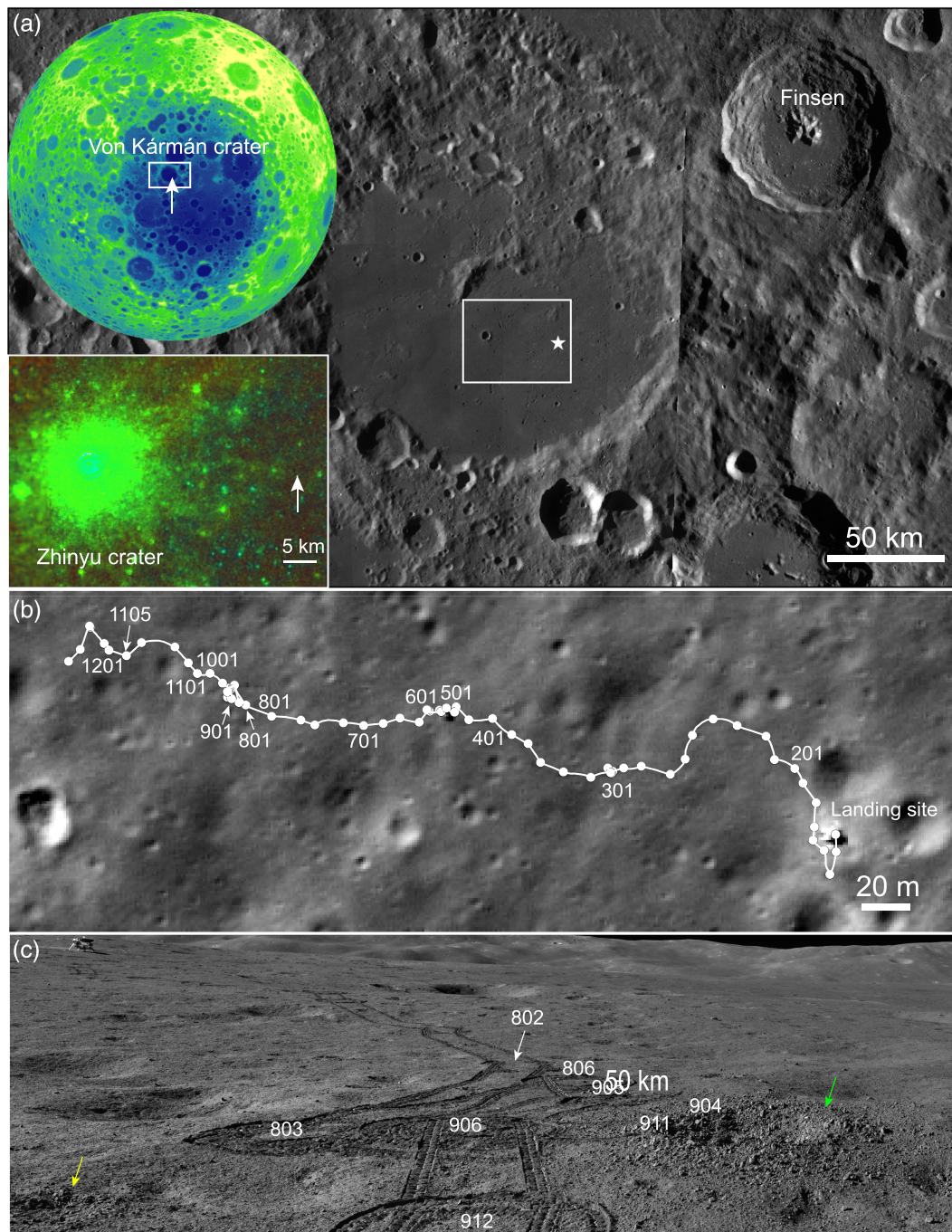


**Figure 1.** Geomorphological context of the Chang'E-4 mission. (a) The Chang'E-4 landing site on the floor of the Von Kármán crater (white star;  $177.588^\circ$  E,  $45.457^\circ$  S). The landing site is positioned in the South Pole—Aitken basin on the farside of the Moon (white box in the upper-left inset; LROC WAC global DTM data set; Scholten et al., 2012). The lower-left inset (Clementine color mosaic; McEwen & Robinson, 1997) shows the Zhinyu crater to the west of the landing site, which has delivered a faint impact ray to the landing site (white arrow). North is up in all the mosaics. (b) The route of the Yutu-2 rover in the first 12 lunar days (white curve). Along the route, numbers along the dots are navigation points that are started with the number of lunar days counted since landing. The base image is from LROC NAC (image number M1311886645LE). North is up. (c) Images obtained at the ninth lunar day by the panoramic camera onboard the Yutu-2 rover. The imaging direction is southwest, and the lander is to the upper left of the panel. The targeted fresh crater is denoted by the green arrow, and another fresh crater is visible nearby (yellow arrow). Both of them are not visible from orbit. Width of wheel track is 15 cm for scale. The denoted numbers are the navigation points around the target crater.

depict a landing area flat in topography (Di et al., 2019), where only few boulders are visible on the surface (Wu et al., 2019). This observation is consistent with orbital data, which depict a highly degraded topography, overall thick regolith cover (Huang et al., 2018), and low-thermal inertia (Figure S1 in the supporting information). The boulder-scarce appearance is further verified by radar observations. The lunar penetrating radar (i.e., LPR; Fang et al., 2014) onboard the Yutu-2 rover has obtained high-quality data along the path. Using the LPR data obtained in the first few lunar days, Lai et al. (2019) and Li et al. (2020) noticed that electromagnetic waves decayed slowly in the top ~10–13 m of the subsurface. Several hyperbolic reflectors were observed in the radargram, which are likely caused by subsurface boulders. The geometry of the hyperbolic reflectors was used to calculate the average relative permittivity and bulk density for this radar-transparent layer, and the results are comparable with those of typical lunar regolith (Lai et al., 2019; Li et al., 2020).

From the sixth lunar day, the rover suddenly encountered several fresh impact craters close to its path. These craters are less than 3 m in diameters and they have exposed thousands of small (less than 10 cm) fragments (e.g., Figure 1c). Both the craters and fragments are in sharp contrast with the otherwise heavily degraded crater population, suggesting a recent emplacement on the surface. This observation is in contrast with both orbital and earlier *in situ* observations, provoking questions about the physical properties of subsurface materials at the landing site, such as potential heterogeneities within lunar regolith. The origin of the fragments is also a basic question to be addressed for interpreting the radar and reflectance spectral data returned by the rover. For example, the rover has obtained reflectance spectra for both the surface regolith and rocky fragments, which were believed to be representative of Finsen's ejecta (Figure 1a; Li et al., 2019; Lin et al., 2019). However, a layer of blocky materials might have been uniformly deposited to the landing area as possibly indicated by the fragments (Figure 1c), so that the reflectance spectra collected are most likely for these distal materials.

The rover performed a detailed investigation for such a fresh crater at the ninth day. The LPR obtained two profiles across the blocky ejecta along different azimuths, and the panoramic camera took multiple photos for the crater at mm-scale resolutions. Here we use data obtained by the LPR to investigate the radar permittivity of subsurface materials beneath and around the blocky ejecta. Images obtained by the panoramic cameras are used to construct millimeter-scale digital terrain models (DTM). Together with data obtained from orbit, the origin of the small fresh craters and the nature of the observed fragments are discussed. Indications to both the geological interpretation of the rover data and impact cratering mechanism are extended.

## 2. Data and Methods

The large-scale geological context of the landing area has been deciphered in previous studies (e.g., Huang et al., 2018; Ling et al., 2019). Here the general morphology of the landing area (Figures 1a and 1b) is shown using images obtained by both the wide-angle camera (WAC) and narrow-angle camera (NAC) of the Lunar Reconnaissance Orbiter Camera (LROC; Robinson et al., 2010). The morphology and topography of the targeted small crater (Figure 1c) are studied using images obtained by the panoramic cameras on the Yutu-2 rover. DTM constructed using photogrammetric methods requires multiple stereo images, and the spatial resolution is usually several times that of the original images, for example, the ~4 m/pixel DTM derived from the ~1.2 m/pixel LROC NAC stereo pairs for the Chang'E-4 landing site (Liu & Wu, 2020). To derive the detailed topography for the target crater, a DTM was built using traditional photogrammetric methods based on stereo pairs obtained by the panoramic cameras (Figure S2a in the supporting information). Integrating this DTM as an input, the shape-from-shading (SfS) method (Horn, 1990) was employed to improve the spatial resolution. The effective resolution of the SfS-derived DTM is 5 mm/pixel (Figure 2b). Methods of implementing SfS and the related uncertainties are introduced in detail by Wu et al. (2018). Note that small blurry areas exist in the DTM because of shadows and difficult view geometries in the panoramic images (e.g., east of the navigation point 906; Figure 2c), where topography reconstruction is prohibited.

The LPR data obtained between the navigation points 904–905 and those between 906–911 are for the blocky ejecta deposit (Figure 2c). During this observation campaign, the rover was driven into the blocky ejecta until reaching the crater rim. Two endeavors of scanning from different directions were accomplished for the blocky ejecta by the LPR (Figure 2c). The LPR system onboard the Yutu-2 rover has a similar design with that on the Yutu rover, and it has two subsystems that are operated at center frequencies of 60 and 500 MHz, respectively (Fang et al., 2014). We only use the high-frequency LPR data here, because the small craters are



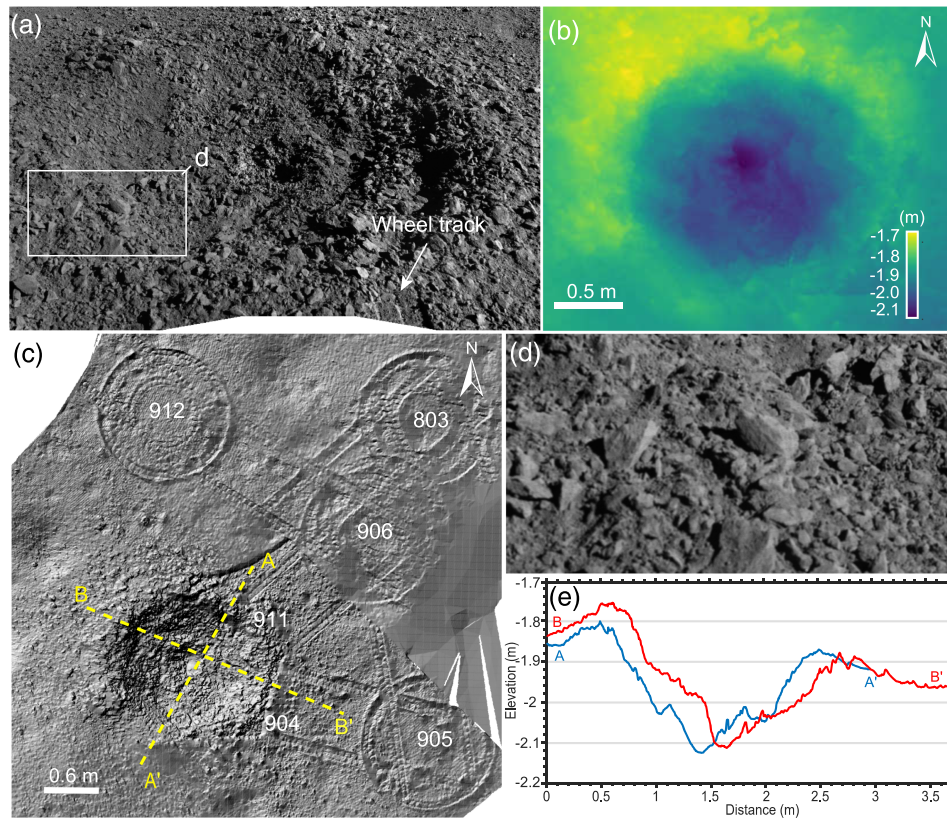


**Figure 2.** Morphology and topography of the small blocky crater inspected by the rover. (a) Large amounts of fragments are visible within and around the small crater. The crater exhibits concentric walls, and high-reflectance materials are visible in the central pit. North is up. (b) High-resolution DTM constructed using the SfS method for the small crater shown in Figure 2b. This crater is  $\sim 2.2$  m in diameter, and the rim-to-floor depth is  $\sim 35$  cm. (c) Shade relief map built for the small crater and the surrounding areas. The base DTM is built using the SfS method, and the crater pointed by the yellow arrow in Figure 1c is not covered. Denoted numbers are the navigation points. (d) Detailed morphology of the dusty fragments. This frame is an enlarged view for the polygonal areas marked in panel (a). (e) Topographic profiles for the small crater show the larger elevation at the northwestern rim. Locations of the two profiles are denoted in panel (c).

$< 3$  m in diameter (Figure 2) and considering their excavation depths are less than a meter, the top few meters of materials are interesting for the purpose of this work. The vertical resolution of the high-frequency LPR data is better than 0.3 m in lunar regolith (Su et al., 2014). The radar data are the level 2B data that were collected in the first 12 lunar days. The standard radar processing procedure (Feng et al., 2017) is employed to process the data, that is, removal of redundant data, dewow filtering, amplitude compensation, background subtraction, and band-pass filtering.

To investigate whether or not the observed fragments originally existed in the subsurface and later been excavated by the small crater, we carry out numerical simulations for the propagation of radar waves in dedicated regolith models. The regolith models were built based on the detailed morphology and geometry of both the small craters and fragments. The 5 mm/pixel resolution DTM allows subtraction of the areal fraction and size frequency distribution of the fragments. Based on the SfS DTM and images obtained by the panoramic cameras, an orthoimage map is constructed for the measurement (Figure S2 in the supporting information). The grid size of the regolith models is set to 1 cm, and the time window is set to 200 ns. The transmitted electromagnetic waves in the models are identical with that transmitted by the high-frequency LPR (Fang et al., 2014). In the regolith models, the depth profile for the relative permittivity of the background regolith follows the method used by Lai et al. (2019). The finite-difference time-domain (Teixeira et al., 1998; Irving & Knight, 2006) method is employed for the numerical simulation which performs differential iteration calculations of the Maxwell's equations to simulate the propagation electromagnetic waves in media.



### 3. Results

Unlike typical bowl-shaped primary craters, the target crater exhibits concentric walls and a central pit (Figure 2). Abundant fragments are visible both within and around this crater, but surfaces beyond ~1 m from the crater rim exhibit few fragments (Figures 1c and 2c). Most of the fragments have angular rims and they are blocky or platy in shapes (Figure 2d). The fragments are earthy in color due perhaps to the heavy dust cover (Figure 2d). It cannot be determined from the appearance alone that whether or not the fragments are crystalline rocks, sintered breccias, and/or just regolith clumps. The fragments are less than 10 cm in the longest dimension, and most of them are less than 5 cm. The areal fraction of recognizable fragments in the DTM is ~10% (Figure S2b in the supporting information). Note that the actual areal fraction of the fragments should be slightly larger, considering that topographic construction is imperfect in some areas (Figure 2d) and fragments less than 5 mm in dimension were not included.

#### 3.1. Radargram Beneath the Blocky Ejecta and the Surrounding Regolith

From the navigation points 802 to 1105, the top ~250 ns of the radargram, which corresponds to ~20 m thick materials in the subsurface can be divided into two layers in terms of echo strengths (Figure 3). A relatively sharp and uneven interface is visible at depths of ~10–13 m in the radargram. Shallower materials have weak echoes and few scatters, and deeper materials exhibit overall stronger echoes (Figure 3). This pattern is generally consistent with that observed by Lai et al. (2019) and Li et al. (2020) for the LPR data obtained in the first five lunar days, supporting the interpretation that the top ~11 m thick materials in the landing area are similar to fine-grained lunar regolith, and deeper materials are blockier.

Within the first layer of the radargram, materials beneath the blocky ejecta (i.e., navigation points 904–905 and 906–911) are indistinguishable from the surrounding normal surfaces where fragments are few (Figure 3). Therefore, the relative permittivity of materials beneath the blocky ejecta is comparable with that of the surrounding normal regolith. The results indicate that either the subsurface materials along the entire rover path are composed of relative homogenous regolith-like materials (Lai et al., 2019; Li et al., 2020) or that small fragments might uniformly exist within the excavation depth of the small crater, but the small sizes of the fragments prohibited strong radar reflections.

#### 3.2. Simulated Radargrams

Regolith models that have the same horizontal and vertical dimensions with the LPR segments for the blocky ejecta are constructed, that is,  $6 \times 15$  m. Referring to the subsurface structures revealed in the top ~200 ns of the radargram (Figure 3), the regolith models assumed different thicknesses of blocky materials in the top 12-m-thick regolith, which is overlain on top of blocky materials at larger depths. The first model (Figure 4a) assumed that the entire upper layer is fragment-free regolith; that is, the simulated materials have grain-sizes less than the grid size of the model (1 cm). Considering that the excavation depth of the target crater is less than the apparent rim-to-floor depth (~35 cm; Figure 2e), the second to fourth regolith models assumed that the top ~30 cm of the first layer is composed of fragment-rich materials (Figures 4b–4d). In the three models, fragments in the shallow subsurface were generated with random shapes. Sizes of the modeled fragments follow a random distribution, and the longest dimensions are from 1–10 cm, which are similar to the size-range of the observed fragments (Figure S2 in the supporting information). The modeled fragments are assumed to have a total areal fraction of ~10% (Figure 4b), 30% (Figure 4c), and 60% (Figure 4d), respectively. To account for the possibility that the fragmental layer is thicker than ~0.3 m, an additional regolith model is set up with a fragmental layer of 1 m thick and the rest of the model design is the same with that shown in Figure 4b. In all the models, the depth profile of relative permittivity is derived based on hyperbolic reflectors observed in the subsurface (Lai et al., 2019), and the fragments were assumed as basaltic in composition that have a typical permittivity of 7.5 (Chung et al., 1970). At depths larger than the fragment layer, an irregularly shaped artificial block that is 10 cm in the longest dimension is implanted as a tracer (Figure 4). This tracer is to produce a hyperbolic reflector in the radargram, and the echo strengths are compared to those formed by the fragment layers.

The observed radargram beneath the blocky ejecta deposits (Figures 4f) is most similar with the first modeled radargram (Figure 4g), which assumed that the first 12 m was composed by fragment-free regolith. A fragment layer that has different assumed thicknesses and/or abundances of rock fragments would uniformly cause strong echoes at depths  $< \sim 50$  ns, which are comparable with those reflected from the

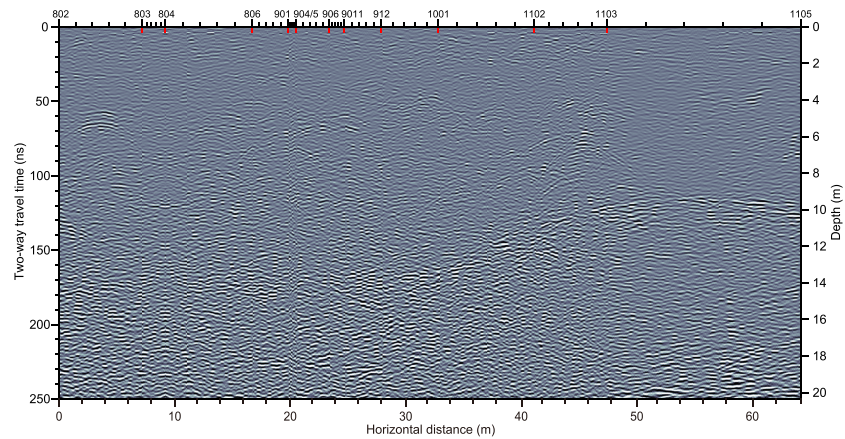


**Figure 3.** Radargram derived by the high-frequency LPR from the eighth to eleventh lunar day. The top ~10–13 m thick materials have weaker echo strengths compared to deeper materials. Numbers at the upper x axis are the navigation points (red ticks). The sections at navigation points 904–905 and 906–911 are for the blocky ejecta (Figure 2c), and the radar echoes are basically the same with those of the surrounding normal regolith. The lower x axis shows the distance sampled by the LPR, which is started from the navigation point 802. The left y axis shows the two-way travel time, and the right y axis denotes depths beneath ground.

buried artificial fragments (Figures 4g–4k). This comparison suggests that most materials beneath the blocky ejecta have grain sizes less than 1 cm, and the observed fragments were not preexisting in the subsurface. The results are consistent with both the orbital observations at different wavelengths (Figures 1b and S1) and the observations by the Yutu-2 panoramic cameras (Figure 1c).

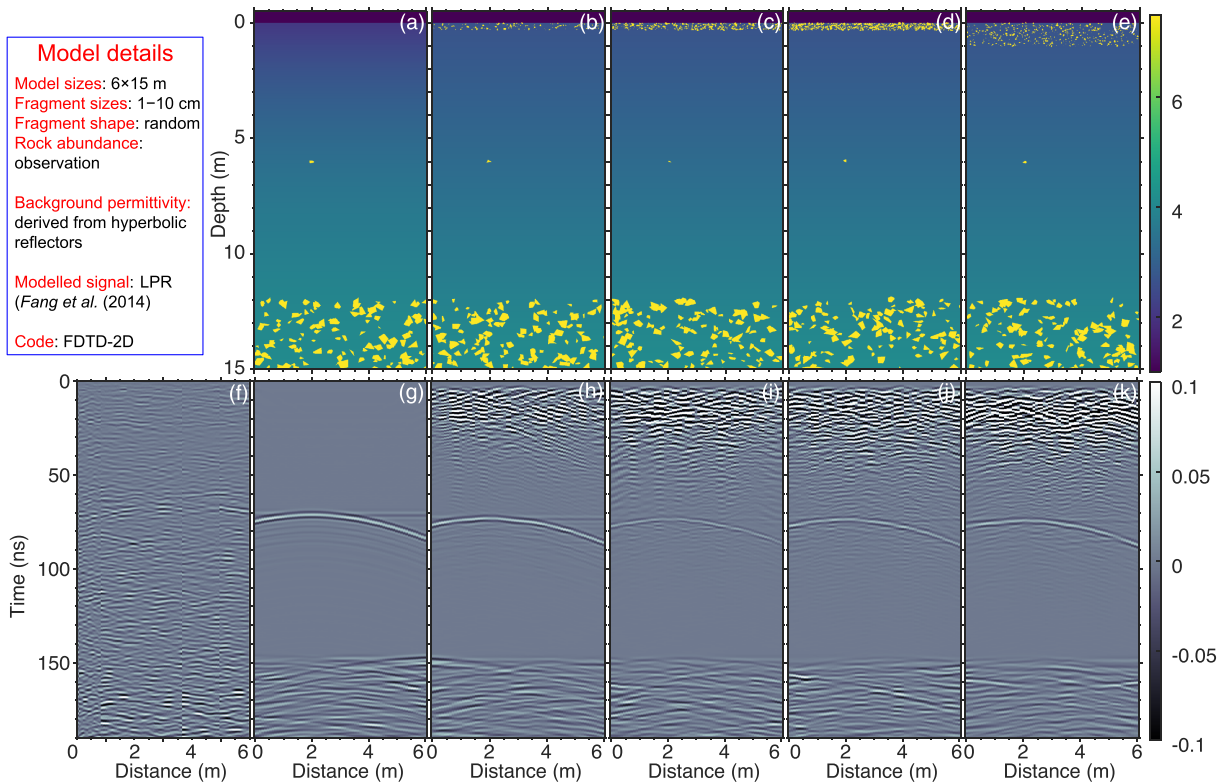


**Figure 4.** Comparison of the observed radargram between the navigation points 904 and 911 and the simulated radargrams. The first row (a–e) shows the model setups, and the color bar denotes the relative permittivity used in the model. Below each model, the simulated radargrams (g–k) are listed, together with the observed radargram (f). The scale bar shows the normalized echo strengths against the peak of the transmitted signal. The comparison suggests that subsurface materials beneath the blocky ejecta should be similar with fragment-free regolith.

## 4. Discussion

### 4.1. Origin of the Small Fresh Craters at the Landing Region

The small fresh crater shown in Figure 2 is not the only one that was encountered by the rover. From Days 6 to 12, at least four such craters are observed along the ~150 m long path, and more are visible at larger distances from the path (Figure S3 in the supporting information). The high spatial density of similar-sized fresh craters in such a small region is not expected for primary craters, considering that the fast overturn rate of surface regolith (Speyerer et al., 2016) and the quick breakdown of small fragments on the lunar surface (McKay et al., 1991) would form continuous transition in the degradation states of similar-sized primary craters. Figure S4 shows the normal appearance of the heavily degraded crater population in this area.

The rover is located in a faint impact ray sourced from the ~3.8 km diameter Zhinyu crater, which is located to the west of the landing site (Figure 1a). Secondaries are frequently visible in impact rays on planetary bodies, and small impact craters on the Moon are efficient enough to deliver large amounts of ejecta to distances that are hundreds of radii of the parent crater (Speyerer et al., 2016). While the small craters shown in Figures 2 and S3 cannot be resolved from orbit due to their small sizes (Figure 1b), larger secondaries are observed in this faint ray of Zhinyu (Figure S5). The high-resolution DTM shows that the northwestern rim of the small crater is higher in elevation than the rest of the crater rim (Figure 2). The observations together suggest that the small blocky craters are most likely secondaries formed by the Zhinyu crater, so that enhanced ejection toward the downrange has caused the larger elevation at the uprange rim of secondaries (Schultz & Gault, 1985).

### 4.2. Origin of the Observed Fragments

The small crater shown in Figure 2 is ~31 km from the center of the Zhinyu crater (Figure 1). Assuming an ejection angle of ~45°, the impact velocity that formed the small crater is ~140 m/s. With such small impact velocities, cratering in porous target is mainly driven by the momentum instead of kinetic energy of the impactor (Schultz & Gault, 1985). The deep pit in the floor of the small crater (Figure 2b) suggests that penetration by projectiles was profound during the cratering process. Based on the different morphological aspects of lunar secondaries (e.g., asymmetric rims and central mounds), laboratory simulations of low-velocity impacts suggested that typical secondaries on the Moon are formed by clusters of fragments instead of single fragments, and most materials excavated by secondaries were local target materials, not the primary ejecta (Schultz & Gault, 1985). The ~0.15 depth-to-diameter ratio of the small crater (Figure 2e) indicates that the projectile delivered from Zhinyu should be highly clustered or single fragment(s), see Figure 13 in Schultz and Gault (1985) for a comparison. Therefore, the shattered projectile(s) that formed the secondaries are a minor portion of the observed fragments (Schultz & Gault, 1985).

During the formation of secondaries, compaction and then ejection of porous surface regolith could be an important source for the observed fragments. On the Moon, lithification of regolith occurs at a wide range of impact velocities due to dynamic loads (Ahrens & Cole, 1974; Kieffer, 1975). At peak pressures larger than ~10 GPa, shock lithification occurs via melting, forming thermally sintered regolith breccia (Spray, 2016). At shock pressures less than ~5 GPa, lithification via melting in lunar regolith is weak, and the major effects of low shock are the collapse of pores and mechanical shortening of grains (Kieffer, 1975). The impacts that formed the secondaries at the landing region were in the subsonic domain, so the peak pressure was restricted below the melting level (Kieffer, 1975), and shock lithification via melting should be very limited, if not at all. On the other hand, physical experiments show that porous materials exhibit inelastic behavior at impact velocities as low as ~20 m/s, and lithification via pore collapse is profound (Scott & Pearce, 1975). Therefore, it is possible that most of the fragments might be formed by impact compaction during the landing of Zhinyu's ejecta, accounting for the earthy appearances (Figure 2d).

The interpretation is in line with previous interpretations that the top 10–13 m thick materials at the landing area are likely regolith (Lai et al., 2019; Li et al., 2020), negating the scenario that there might be a recent uniform deposition of fragments across the landing area. The visible-to-near-infrared spectrometer onboard the Yutu-2 rover has acquired reflectance spectra around this crater. The proposed origin of the fragments could be tested and intergraded in the compositional analyses for the spectral data, for example, most fragments should have exhibit similar spectra with the surrounding regolith. On the other hand, the ubiquitous occurrences of secondaries on the Moon suggest that compaction caused by secondary impact might have



been common in lunar history, hinting that secondary impacts might have been an efficient process to form fragments from lunar regolith, increasing the local porosity (Short, 1966).

## 5. Conclusions

Several blocky craters are observed along the path of the Yutu-2 rover. The rover performed a detailed observation for a blocky crater at the ninth lunar day, permitting detailed morphological, geometrical, and radar scattering studies for the fragments. Radargram obtained by the high-frequency lunar penetrating radar across the blocky ejecta are indistinguishable from the surrounding normal surfaces that are depleted with surface fragments. Numerical simulations for the propagation of radar waves in high-resolution regolith models suggest that the fragments were not existing in the preimpact subsurface. The blocky craters are located in an impact ray from the Zhinyu crater, and the rims toward Zhinyu are more elevated. These observations are consistent with the high spatial density of this crater population, suggesting that the fresh craters are secondaries of Zhinyu. The fragments are likely dominated by impact-lithified regolith clumps, with additional contribution from the shattered primary ejecta that formed the secondaries. The origin of the fragments is indicative to the interpretation of both the regional stratigraphy and provenances of surface materials detected by the mission.

## Acknowledgments

We thank the efforts of the engineering team of the Chang'E-4 mission. The two anonymous reviewers provided helpful comments to improve the manuscript. The LRO data reported in this study are available from PDS. Data obtained by the LPR and panoramic camera in the first 2 lunar days have been released (<http://moon.bao.ac.cn/>), and those used in this study will be released to the same archive after 12 months of internal investigation. The DTM constructed using the SFS method, the processed radar data, and the regolith models are available at <http://doi.org/10.5281/zenodo.3706469>. The FDTD-2D simulations follow the method of Irving and Knight (2006/2006). The authors are supported by the B-type Strategic Priority Program of the Chinese Academy of Sciences (XDB41000000), the National Natural Science Foundation of China (41773063, 41525015, and 41830214), the Science and Technology Development Fund of Macau (0042/2018/A2), and the Pre-research Project on Civil Aerospace Technologies (D020101) of CNSA.

## References

- Ahrens, T., & Cole, D. M. (1974). Shock compression and adiabatic release of lunar fines from Apollo 17. Paper presented at the Lunar and Planetary Science Conference Proceedings.
- Chung, D. H., Westphal, W. B., & Simmons, G. (1970). Dielectric properties of Apollo 11 lunar samples and their comparison with Earth materials. *Journal of Geophysical Research*, *75*(32), 6524–6531. <https://doi.org/10.1029/JB075i032p06524>
- Di, K., Liu, Z., Liu, B., Wang, W., Peng, M., Wang, Y., et al. (2019). Chang'e-4 lander localization based on multi-source data. *Journal of Remote Sensing*, *23*(1), 181–184. <https://doi.org/10.11834/jrs.20199015>
- Fang, G., Zhou, B., Ji, Y., Zhang, Q., Shen, S., Li, Y., et al. (2014). Lunar penetrating radar onboard the Chang'e-3 mission. *Research in Astronomy and Astrophysics*, *14*(12), 1607–1622. <https://doi.org/10.1088/1674-4527/14/12/009>
- Feng, J., Su, Y., Ding, C., Xing, S., Dai, S., & Zou, Y. (2017). Dielectric properties estimation of the lunar regolith at CE-3 landing site using lunar penetrating radar data. *Icarus*, *284*, 424–430. <https://doi.org/10.1016/j.icarus.2016.12.005>
- Horn, B. K. P. (1990). Height and gradient from shading. *International Journal of Computer Vision*, *5*(1), 37–75. <https://doi.org/10.1007/bf00056771>
- Huang, J., Xiao, Z., Flahaut, J., Martinot, M., Head, J., Xiao, X., et al. (2018). Geological characteristics of Von Kármán crater, northwestern south pole-Aitken Basin: Chang'E-4 landing site region. *Journal of Geophysical Research: Planets*, *123*, 1684–1700. <https://doi.org/10.1029/2018JE005577>
- Irving, J., & Knight, R. (2006). Numerical modeling of ground-penetrating radar in 2-D using MATLAB. *Computers & Geosciences*, *32*(9), 1247–1258. <https://doi.org/10.1016/j.cageo.2005.11.006>
- Kieffer, S. W. (1975). From regolith to rock by shock. *The Moon*, *13*(1–3), 301–320. <https://doi.org/10.1007/bf00567522>
- Lai, J., Xu, Y., Zhang, X., Xiao, L., Yan, Q., Meng, X., et al. (2019). Comparison of dielectric properties and structure of lunar regolith at Chang'e-3 and Chang'e-4 landing sites revealed by ground penetrating radar. *Geophysical Research Letters*, *46*, 12783–12793. <https://doi.org/10.1029/2019GL084458>
- Li, C., Liu, D., Liu, B., Ren, X., Liu, J., He, Z., et al. (2019). Chang'e-4 initial spectroscopic identification of lunar far-side mantle-derived materials. *Nature*, *569*(7756), 378–382. <https://doi.org/10.1038/s41586-019-1189-0>
- Li, C., Su, Y., Pettinelli, E., Xing, S., Ding, C., Liu, J., et al. (2020). The Moon's farside shallow subsurface structure unveiled by Chang'e-4 lunar penetrating radar. *Science Advances*, *6*(9), eaay6898. <https://doi.org/10.1126/sciadv.aay6898>
- Lin, H., He, Z., Yang, W., Lin, Y., Xu, R., Zhang, C., et al. (2019). Olivine-norite rock detected by the lunar rover Yutu-2 likely crystallized from the SPA impact melt pool. *National Science Review*. <https://doi.org/10.1093/nsr/nwz183>
- Ling, Z., Qiao, L., Liu, C., Cao, H., Bi, X., Lu, X., et al. (2019). Composition, mineralogy and chronology of mare basalts and non-mare materials in Von Kármán crater: Landing site of the Chang'e-4 mission. *Planetary and Space Science*, *179*, 104,741. <https://doi.org/10.1016/j.pss.2019.104741>
- Liu, W., & Wu, B. (2020). An integrated photogrammetric and photoclinometric approach for illumination-invariant pixel-resolution 3D mapping of the lunar surface. *ISPRS Journal of Photogrammetry and Remote Sensing*, *159*, 153–168. <https://doi.org/10.1016/j.isprsjprs.2019.11.017>
- McEwen, A., & Robinson, M. (1997). Mapping of the Moon by Clementine. *Advances in Space Research*, *19*(10), 1523–1533. [https://doi.org/10.1016/S0273-1177\(97\)00365-7](https://doi.org/10.1016/S0273-1177(97)00365-7)
- McKay, D. S., Heiken, G., Basu, A., Blanford, G., Simon, S., Reedy, R., et al. (1991). The lunar regolith. In G. H. Heiken, D. T. Vaniman, & B. M. French (Eds.), *Lunar sourcebook: A user's guide to the Moon*, (pp. 285–356). Cambridge: Cambridge University Press.
- Robinson, M. S., Brylow, S. M., Tschimmel, M., Humm, D., Lawrence, S. J., Thomas, P. C., et al. (2010). Lunar Reconnaissance Orbiter Camera (LROC) instrument overview. *Space Science Reviews*, *150*, 81–124.
- Scholten, F., Oberst, J., Matz, K., Roatsch, T., Wählisch, M., Speyerer, E., & Robinson, M. (2012). GLD100: The near-global lunar 100 m raster DTM from LROC WAC stereo image data. *Journal of Geophysical Research*, *117*, E00H17. <https://doi.org/10.1029/2011JE003926>
- Schultz, P., & Gault, D. E. (1985). Clustered impacts: Experiments and implications. *Journal of Geophysical Research*, *90*(B5), 3701–3732. <https://doi.org/10.1029/JB090iB05p03701>
- Scott, R., & Pearce, R. W. (1975). Soil compaction by impact. *Géotechnique*, *25*(1), 19–30. <https://doi.org/10.1680/geot.1975.25.1.19>
- Short, N. M. (1966). Shock-lithification of unconsolidated rock materials. *Science*, *154*(3747), 382–384. <https://doi.org/10.1126/science.154.3747.382>

- Speyerer, E., Povilaitis, R., Robinson, M., Thomas, P., & Wagner, R. (2016). Quantifying crater production and regolith overturn on the Moon with temporal imaging. *Nature*, *538*(7624), 215–218. <https://doi.org/10.1038/nature19829>
- Spray, J. G. (2016). Lithification mechanisms for planetary regoliths: The glue that binds. *Annual Review of Earth and Planetary Sciences*, *44*(1), 139–174. <https://doi.org/10.1146/annurev-earth-060115-012203>
- Su, Y., Fang, G., Feng, J., Xing, S., Ji, Y., Zhou, B., et al. (2014). Data processing and initial results of Chang'e-3 lunar penetrating radar. *Research in Astronomy and Astrophysics*, *14*(12), 1623–1632. <https://doi.org/10.1088/1674-4527/14/12/010>
- Teixeira, F., Weng, C., Straka, M., Oristaglio, M., & Wang, T. (1998). Finite-difference time-domain simulation of ground penetrating radar on dispersive, inhomogeneous, and conductive soils. *IEEE Transactions on Geoscience and Remote Sensing*, *36*(6), 1928–1937. <https://doi.org/10.1109/36.729364>
- Wu, B., Liu, W. C., Grumpe, A., & Wöhler, C. (2018). Construction of pixel-level resolution DEMs from monocular images by shape and albedo from shading constrained with low-resolution DEM. *ISPRS Journal of Photogrammetry and Remote Sensing*, *140*, 3–19. <https://doi.org/10.1016/j.isprsjprs.2017.03.007>
- Wu, W., Li, C., Zuo, W., Zhang, H., Liu, J., Wen, W., et al. (2019). Lunar farside to be explored by Chang'e-4. *Nature Geoscience*, *12*(4), 222–223. <https://doi.org/10.1038/s41561-019-0341-7>